

Magnetic ground state of distorted 6H perovskite $\text{Ba}_3\text{CdIr}_2\text{O}_9$

Md Salman Khan,¹ Abhisek Bandyopadhyay,¹ Abhishek Nag,¹ Vinod Kumar,² A. V. Mahajan,² and Sugata Ray^{1,3,*}

¹*School of Materials Science, Indian Association for the Cultivation of Science,
2A & 2B Raja S. C. Mullick Road, Jadavpur, Kolkata 700032, India*

²*Department of Physics, Indian Institute Of
Technology Bombay, Powai, Mumbai 400076, India*

³*Technical Research Center, Indian Association for the Cultivation of Science,
2A & 2B Raja S. C. Mullick Road, Jadavpur, Kolkata 700032, India*

(Dated: August 15, 2019)

Abstract

Perovskite iridates of 6H hexagonal structure present a plethora of possibilities in terms of the variety of ground states resulting from a competition between spin-orbit coupling (SOC), hopping, noncubic crystal field ($\Delta_{\text{CFE}}^{\text{NC}}$) and superexchange energy scales within the Ir_2O_9 dimers. Here we have investigated one such compound $\text{Ba}_3\text{CdIr}_2\text{O}_9$ by x-ray diffraction, *dc* magnetic susceptibility (χ), heat capacity (C_p) and also ^{113}Cd nuclear magnetic resonance (NMR) spectroscopy. We have established that the magnetic ground state has a small but finite magnetic moment on Ir^{5+} in this system, which likely arises from intradimer Ir-Ir hopping and local crystal distortions. Our heat capacity, NMR, and *dc* magnetic susceptibility measurements further rule out any kind of magnetic long-/short range ordering among the Ir moments down to at least 2K. In addition, the magnetic heat capacity data shows linear temperature dependence at low temperatures under applied high fields (> 30 kOe), suggesting gapless spin-density of states in the compound.

I. INTRODUCTION

5d transition metal oxides, especially iridates, have become a fertile ground for hosting diverse spectrum of exotic physical properties due to the intricate competition between spin-orbit coupling (SOC), crystal field energy (Δ_{CFE}), and on-site Coulomb repulsion (U)¹⁻⁹. In contrast to the traditional wisdom of uncorrelated band metallicity in iridates due to extended 5d orbitals, B.J.Kim *et al.* first established the central role of SOC on the Mott insulating ground state in the layered tetravalent iridate Sr_2IrO_4 ⁷. Extension of the same idea to pentavalent iridates (Ir^{5+} : $5d^4$) gives rise to different situations. Substantial SOC (λ) in Ir^{5+} produces ${}^6C_4 = 15$ possible J states or organisations of electrons within the 6 t_{2g} orbitals, with $J = 0$ as the ground state¹⁰. But a purely nonmagnetic $J = 0$ state has not been encountered till date in any of the reported $5d^4$ iridate systems¹¹⁻¹⁴. It has been speculated that the magnetism in these d^4 compounds may arise from the Van Vleck-type intrasite singlet-triplet excitations ($J = 0 \rightarrow J = 1$) when the superexchange (mediated by complex Ir-O-Ir paths) energy scale of $4t^2/2U$ becomes comparable to SOC-induced singlet-triplet energy gap, allowing virtual transitions to higher levels and magnetic condensation of Van Vleck excitons¹⁰. On the other hand, solid state effects such as large bandwidth of the 5d orbitals, ligand-Ir charge transfer, non-cubic crystal field and intersite Ir-Ir hopping always act against the atomic SOC effect. Moreover, Ir-Ir hopping can modify the ground state itself by creating several mixed J states and a finite moment for which excitonic mechanisms are not relevant¹⁵. Of course the other possibility is that these all effectively reduce the SOC strength (λ) on the Ir-site and as a result, spontaneous magnetic moments may be generated¹⁶⁻²³. The closest realization of non-magnetic $J = 0$ ground state in the d^4 systems till date is recorded in the $6H$ hexagonal perovskite compound $\text{Ba}_3\text{ZnIr}_2\text{O}_9$ where a tiny moment of $0.2\mu_B/\text{Ir}$ appears on each Ir^{5+} site due to strong intradimer hopping mechanism within a Ir_2O_9 dimer unit²⁴.

Here, in this paper we report a new compound $\text{Ba}_3\text{CdIr}_2\text{O}_9$ (BCIO) which belongs to the family of $6H$ hexagonal perovskite $\text{Ba}_3M\text{Ir}_2\text{O}_9$ ($M =$ alkaline earth or rare earth element). Although rigorous experimental studies have been performed on the $6H$ $\text{Ba}_3M\text{Ir}_2\text{O}_9$ compounds with $M = \text{Zn, Mg, Ca, Sr, Y, Sc}$ and In ²⁴⁻²⁸, showing diverse ground state properties, the $M = \text{Cd}$ member has not been carefully looked at, except an earlier report describing only the synthesis and structural details of the compound²⁵.

The standard $6H$ hexagonal structure consists of a single MO_6 octahedron and Ir_2O_9 dimers of two face sharing IrO_6 octahedra [Fig.1(e)]. The Ir-Ir structural dimers are constructed parallel to the crystallographic c -axis and these dimers are linked with each other to form an edge-shared triangular lattice of Ir atoms in the $a - b$ plane [Fig.1(c)]. Such geometries next dictate how the tiny Ir spins should interact with each other which is an outcome of different Ir-Ir exchange interactions²⁶, as displayed by blue curved arrows in Fig. 1(b) and 1(c) and by blue dashed lines in Fig. 1(d). Also, the local octahedral distortions influencing the Ir-O bond lengths and Ir-O-Ir bond angles further complicate the magnetic ground state in this system. A. Nag *et al.*²⁶ has shown that the competition between SOC and octahedral distortions in $Ba_3M Ir_2O_9$ ($M = Mg, Ca, Sr$) series of compounds greatly influences the magnetic properties. Due to similar ionic radii of Mg and Zn, the $M=Mg$ compound bears closer analogy to the spin orbital liquid $Ba_3ZnIr_2O_9$ ²⁴, while $M = Ca$ and Sr compounds, due to higher degree of monoclinic ($C2/c$) structural distortions, reveal differences in magnetic behaviour. Although the amount of octahedral distortion was not monotonic with the ionic radius of M cations, interdimer Ir-Ir distance increases and intradimer Ir-Ir distance decreases regularly with increasing M^{2+} cation size²⁶. The $6H$ -hexagonal perovskite $Ba_3CdIr_2O_9$ becomes particularly important in this context where Cd^{2+} has ionic radius close to Ca ($r_{Ca^{2+}} = 1.00 \text{ \AA}$) but in between the Mg ($r_{Mg^{2+}} = 0.72 \text{ \AA}$) and Sr ($r_{Sr^{2+}} = 1.18 \text{ \AA}$).

Another salient notion for looking at the $Ba_3CdIr_2O_9$ compound is that unlike $M = Zn, Mg, Ca$ and Sr compounds, the Cd counterpart has an NMR active ^{113}Cd ($I = 1/2$) nucleus with reasonable natural abundance. Therefore, ^{113}Cd NMR becomes an exciting option to explore the local spin dynamics around Ir in this compound. Keeping this in mind, here in this paper we have investigated the $6H$ $Ba_3CdIr_2O_9$ compound using standard X-ray diffraction (XRD), X-ray photoelectron spectroscopy (XPS), electric resistivity, dc magnetic susceptibility, heat capacity, and ^{113}Cd NMR measurements. Our combined dc susceptibility and NMR studies confirm the true intrinsic nature of the developed tiny Ir-moments ($\mu_{eff} = 0.3 \mu_B/Ir$) in this compound. Despite having considerable antiferromagnetic (AFM) interaction ($\Theta_{CW} = -21 \text{ K}$) between these Ir^{5+} moments, the $Ba_3CdIr_2O_9$ compound does not order down to at least 2 K (frustration parameter > 10), due to geometric frustration arising from the triangular lattice [Fig. 1(c)-(d)], which is markedly different from $M = Ca, Sr$ compounds. Further, the magnetic heat capacity reveals a linear temperature dependence

at low- T unfolding the gapless nature of spin excitations within this compound.

II. EXPERIMENTAL METHODS

Polycrystalline samples of $\text{Ba}_3\text{CdIr}_2\text{O}_9$ were prepared by standard solid state reaction methods using high purity (>99.9%) starting materials BaCO_3 , CdO , IrO_2 (from Sigma Aldrich) in an appropriate ratio. These mixtures were thoroughly ground and pressed into pellets before initial calcination at 800°C for 12h. Finally the as-calcined pellet was annealed at 1100°C four times for 12 hours each in air with several intermediate grindings. The phase purity of the sample was checked from X-ray powder diffraction measured at Rigaku Smartlab x-ray diffractometer with $\text{Cu } K_\alpha$ radiation at room temperature as well as low temperatures. The crystal structure of this sample was obtained after refining the XRD data by Rietveld technique using FULLPROF program²⁹. To check homogeneity and stoichiometry in the sample, Energy Dispersive X-Ray Analysis (EDX) was also performed using Field Emission Scanning Electron Microscope (FE-SEM, JEOL, JSM-7500F). Temperature dependent electrical resistivity was measured using the four probe technique in a laboratory based experimental set up. The X-ray photoelectron spectroscopy (XPS) measurements were carried out using OMICRON electron spectrometer, equipped with SCIENTA OMICRON SPHERA analyzer and $\text{Al } K_\alpha$ monochromatic source with an energy resolution of 0.5 eV. The sample surface has been cleaned before experiment by *in-situ* Ar-sputtering. The collected spectra were then processed and analyzed with Kolxpd program. The temperature and magnetic field dependent dc magnetization was carried out using the Quantum Design (SQUID) magnetometer. Heat capacity both in zero field and several higher magnetic fields (upto 9 Tesla) were measured using the heat capacity attachment of a Quantum Design PPMS. Measurements of the ^{113}Cd (nuclear spin $I = 1/2$, natural abundance 12.26 %, and gyromagnetic ratio $\gamma/2\pi = 9.028 \text{ MHz/Tesla}$) NMR spectra and spin-lattice relaxation rate ($1/T_1$) were performed as a function of temperature in a fixed field magnet ($H = 93.9543 \text{ kOe}$) with a room-temperature bore, using standard pulse NMR techniques. The temperature was varied in the range 4-300 K using an Oxford continuous flow cryostat.

III. RESULTS AND DISCUSSIONS

A. Crystal structure from XRD

Rietveld refinement of the collected XRD pattern [Fig. 1(a)-(I) for $T = 300$ K] ensures nearly single phase with monoclinic $C2/c$ space group for $\text{Ba}_3\text{CdIr}_2\text{O}_9$, except only very small proportion ($< 1\%$) of unidentified nonmagnetic impurity phase [marked by asterisks in Fig. 1(a)-(I)]. Further, the Energy dispersive X-Ray analysis ensures that the sample is chemically homogeneous and stoichiometry is nearly retained in the target composition, *i.e.*, Ba:Cd:Ir has been found to be very close to 3:1:2, within the given accuracy of the measurement. Similar to the $M = \text{Ca}$ and Sr cases²⁶ the refined crystal structure [Fig. 1(b)] of the Cd compound comprises a larger unit cell, compared to the higher symmetry $P6_3/mmc$ space group of $M = \text{Zn}$ and Mg counterparts^{24,26}, in order to accommodate the bigger sized Cd cation. Further careful analysis strongly refutes any Cd/Ir anti-site disorder due to significant ionic size mismatch between Cd^{2+} and Ir^{5+} . Like $6H$ hexagonal perovskites, the Ir ions of this structure form Ir_2O_9 dimers [Fig. 1(e)], while Cd ions occupy the isolated octahedral sites sharing corners with the Ir_2O_9 dimers on either side of the c -axis. The refined lattice parameters, atomic coordinates, site occupancies along with the goodness factors are summarized in Table-1. Next, we have performed low temperature XRD measurements and consequently, the refined XRD data at $T = 4$ K is displayed in Fig. 1(a)-(II). Excepting the usual lattice contraction with decreasing temperature, the structure and symmetry remained the same. However, one important observation has been a clear reduction in coordination asymmetry around Ir at 4 K, *i.e.* the difference between two Ir-O2 bond lengths has got substantially reduced (see Table-2). Due to lower symmetry monoclinic space group, $\text{Ba}_3\text{CdIr}_2\text{O}_9$, like Ca/Sr analogues, has 5 different O sites [Fig. 1(e) and Table-1]. This causes six different Ir-O bond lengths, and thus, multiple dissimilar Ir-O-Ir bond angles which should modify the Ir-O-Ir magnetic exchange pathways in this compound. The IrO_6 octahedral units within the Ir_2O_9 dimers are also rotated with respect to each other as a result of monoclinic distortion, as is evident from Fig. 1(c), where O ions are not aligned on top of each other along the c -axis. The effect of local non-cubic crystal field ($\Delta_{\text{CFE}}^{\text{NC}}$) around each Ir ion due to five types of oxygen and also monoclinic

symmetry driven stronger rotational distortions within IrO_6 octahedra units should lift the t_{2g} degeneracy completely for this compound, as for the Ca and Sr ones²⁶. On top of it, two interesting aspects in the context of BCIO structure are as follows:

i) The intradimer Ir-Ir distance (2.75 Å) of the Cd compound closely matches with the Mg analogue but is longer than the Ca/Sr counterparts²⁴. This might cause weakening in intradimer Ir-Ir exchange interactions, compared to the Ca/Sr systems.

ii) The Ir_2O_9 dimers create almost equilateral triangular units in the a - b plane and along c axis [see Fig. 1(c)-(d)], giving rise to several triangular antiferromagnetic interactions. The more symmetric triangular units generate higher degree of frustration in the title compound, exactly like Zn and Mg counterparts²⁴ but unlike the Ca and Sr analogs²⁶ where higher asymmetry in the Ir-triangles reduces frustration.

Therefore, the magnetic ground state in $\text{Ba}_3\text{CdIr}_2\text{O}_9$ resembles more with the $M = \text{Zn}$ and Mg compounds, even though the $M = \text{Cd}$ compound possesses an overall lattice symmetry like the Ca, Sr counterparts.

B. Ir-oxidation state and Electronic property

Estimation of the iridium valence is of central importance in understanding the magnetic ground state of these $5d$ iridates, as the $\text{Ir}^{4+}/\text{Ir}^{6+}$ species are magnetic^{7,30-32} while the Ir^{5+} ion should be ideally non magnetic ($J = 0$). Therefore, to confirm the oxidation state of Ir in our $\text{Ba}_3\text{CdIr}_2\text{O}_9$ compound, Ir $4f$ core level XPS spectrum was collected and fitted using a single spin orbit split doublet [Top left inset to Fig. 2(a)]. The energy positions of $4f_{7/2}$ (63.10 eV) and $4f_{5/2}$ (66.15 eV) doublets along with their spin orbit separation around 3.05 eV, confirm pure 5^+ charge state of Ir in this compound^{24,26,33,34}. In such a scenario, without the effect of SOC this system should become metallic in a conventional band picture⁷. To verify this, valence band photoemission spectrum was further collected as shown in the Fig 2(a). As displayed in the top right inset of Fig. 2(a), absence of the density of states right at the fermi level, confirms the insulating behavior of this material. To further check the gapped nature of this compound electrical resistivity has been measured using a standard four probe technique. The temperature dependence of electrical resistivity also supports the insulating behaviour in the entire measured temperature range with 128.5 Ohm-cm at room temperature, and by 120 K it exceeds 10^5 Ohm-cm of resistivity. Although insulating, the

resistivity does not follow a thermally activated exponential behaviour $\rho = \rho_0 \exp(E_p/k_B T)$ as expected for a simple semiconductor³⁵. Rather it can be fitted by Mott's variable range hopping (VRH) model in two dimension with $\rho = \rho_0 \exp(T_0/T)^{1/3}$.

C. Magnetic Susceptibility

We have further examined the bulk *dc* magnetic behaviour of this material. Temperature dependence of both zero field cooled (ZFC) and field cooled (FC) *dc* magnetic susceptibilities (χ vs *T*) have been recorded in the temperature range of 2-300 K, as illustrated in Fig. 3(a). The nearly featureless paramagnetic-like susceptibility curve in the entire temperature range suggests no sign of magnetic long-range ordering in this compound, consistent with several other *d*⁴ iridates^{15,26}. In addition, a kink-like feature is seen at around 50 K. An anomaly at about 50 K is sometimes present due to oxygen condensed on the sample. In the present case, we flushed the sample space with helium gas at 350 K several times but the anomaly still remained. Therefore, there is a possibility that the feature is intrinsic and appearing due to short-range magnetic interactions present in the system. Further, the ZFC-FC divergence starts to develop from ~ 250 K in lower applied fields (data not shown in the figure) and gets completely suppressed under the application of higher magnetic fields, probably indicating the presence of a small fraction of frozen spins^{36,37} in this compound. Magnetic field dependence of *dc* magnetization (*M* versus *H*) has also been measured at 2 K and 300 K and are shown in Fig. 3(b). The absence of any coercivity and remnant magnetization in the 2 K *M* vs *H* data strongly refutes hysteresis like behavior, and consequently, possibility of ferromagnetic interactions in this sample. The observed slight nonlinearity at very low fields has been commonly found in several *d*⁴ iridate system^{12,13,38}. In all these works, the similar nonlinear *M* vs *H* curves (not hysteresis) did not represent any ferromagnetic components either.

We have analyzed the susceptibility (in an applied field of 10 kOe) data using the Curie-Weiss (C-W) equation $\chi = \frac{C}{T - \Theta_{CW}} + \chi_0$ (*C* is the Curie constant while Θ_{CW} and χ_0 represent the Curie-Weiss temperature and the temperature independent susceptibility, respectively). Note that given the weak *T*-dependence of the susceptibility, there is always some uncertainty about the obtained Curie-Weiss fitting parameters which depend on the temperature range of fitting and also on the applied magnetic fields, similar to other Iridate quantum spin

liquids³⁹. The key point here is to have an applied magnetic field which should be strong enough to suppress unsaturated paramagnetic components while retaining all existing short range correlations. Under this consideration the 10 kOe *dc* susceptibility versus temperature data [$1/(\chi - \chi_0)$ versus T plot, shown in the inset of Fig. 3(a)] appears to be most reasonable for fitting. Our fitting yields a Θ_{CW} value of around -21 K and an effective magnetic moment $\mu_{eff} \sim 0.3 \mu_B/\text{Ir}$, a closer analogy to the 6H $\text{Ba}_3\text{ZnIr}_2\text{O}_9$ compound²⁴. This small finite value of magnetic moment on individual Ir^{5+} site could develop due to intersite real Ir-Ir hopping via Ir-O-Ir paths within Ir_2O_9 dimers causing delocalization of holes and thus, deviating from a perfect individual atomic $J = 0$ arrangement²⁶. Also, local non cubic crystal distortions around the IrO_6 octahedral unit may cause mixing of $J = 0$ singlet with $J = 1$ triplet state^{17,18}, and consequently give rise to excitonic moments. The moderate negative value of Θ_{CW} suggests antiferromagnetic interaction between the Ir^{5+} moments. Such AFM correlations among the Ir^{5+} moments within the triangular network [Fig. 1(c)] of $\text{Ba}_3\text{CdIr}_2\text{O}_9$ compound gives rise to magnetic frustration which possibly prevents the system to order. Absence of magnetic ordering with a negative Θ_{CW} has been considered as one of the signatures of QSL^{36,37}. In this context our $\text{Ba}_3\text{CdIr}_2\text{O}_9$ compound might be proposed as a potential QSL candidate, **like $M = \text{Zn}$ and Mg counterparts**^{24,26}. Clearly, *dc* magnetic susceptibility of $\text{Ba}_3\text{CdIr}_2\text{O}_9$ is quite different from $M = \text{Sr}$ and Ca analogues, which exhibit weak ferromagnetic upturn and a dimer like feature respectively along with strong magnetic interactions²⁶.

D. Heat capacity

The magnetic frustration of a disordered material is expressed by the amount of magnetic entropy retained within the system at very low temperatures. To further check the magnetic ground state and also to explore the nature of magnetic excitations in $\text{Ba}_3\text{CdIr}_2\text{O}_9$, we have performed heat capacity measurements (C_p versus T) on this sample at zero field and several applied magnetic fields, and the obtained results are displayed in Fig. 4(a). Absence of any sharp λ -like anomaly in all the measured C_p versus T data [Fig. 4(a)] strongly negates existence of long-range magnetic order and/or structural phase transitions. Although a weak kink-like feature is present at ~ 50 K in the temperature dependent *dc* susceptibility [Fig. 3(a)] for this sample, absence of any corresponding signature in heat capacity suggests

very feeble magnetic interactions. But, a weak hump-like feature is seen below ~ 10 K in the C_p versus T data, which gets shifted towards higher T -values gradually with increasing magnetic field [Fig. 4(a)]. This suggests a two-level Schottky anomaly, possibly arising from some proportion of paramagnetic centers^{37,40}. The total C_p is thus modeled as the sum of three contributions, namely, the lattice part ($C_{lattice}$), the magnetic contribution (C_M) from correlated magnetic moments, and the two-level Schottky anomaly (C_{sch}).

In absence of a suitable nonmagnetic analogue, $C_{lattice}$ for this sample was extracted after fitting the C_p data in the T range 70-300 K with the Debye-Einstein equation assuming one Debye term and two Einstein terms. The fitted curve was then extrapolated down to the lowest measuring T [inset to Fig. 4(a)] and taken as the $C_{lattice}$. After subtracting $C_{lattice}$ from the total C_p , finally the heat capacity of the sample is left out with ($C_M + C_{sch}$). Now, in order to get the intrinsic magnetic heat capacity C_M , ‘two-level Schottky anomaly’ analysis has been performed taking the following strategy: first we subtract the zero field C_p data, *i.e.*, $C_p(H = 0)$ from those in the applied magnetic fields, *i.e.*, $C_p(H \neq 0)$. Consequently, the temperature dependence of this difference ($\Delta C_{p,mag}/T$), as illustrated in Fig. 4(b), has been fitted with two-level Schottky anomaly equation,

$$\frac{\Delta C_{p,mag}}{T} = \frac{f}{T} [C_{sch}(\Delta(H \neq 0)) - C_{sch}(\Delta(H = 0))] \quad (1)$$

where, f is the percentage of paramagnetic centers in the sample; $C_{sch}(\Delta)$ and $C_{sch}(\Delta_0)$ are the Schottky contributions to the specific heat at applied magnetic fields and zero field respectively, while $\Delta(H)$ is the Zeeman splitting in applied magnetic field and Δ_0 represents energy separation between the two levels at $H = 0$. The $C_{sch}(\Delta)$ is further defined as,

$$C_{sch}(\Delta) = R \left(\frac{\Delta}{k_B T} \right)^2 \frac{\exp(\Delta/k_B T)}{(1 + \exp(\Delta/k_B T))^2} \quad (2)$$

The corresponding Schottky fits (shown in Fig.4(b)) yield $f \approx 0.5-0.8\%$, indicating very small fraction of isolated magnetic centers in this sample. The two-level Schottky gap $\frac{\Delta}{k_B}$ follows a linear relation with applied magnetic field $\Delta = g\mu_B H$ [inset of Fig.4(b)], consistent with the scenario of free spin Schottky anomalies^{37,40}. The estimated g value from this linear fit is ≈ 1.42 .

Finally, the magnetic specific heat C_M is plotted against temperature after eliminating both the lattice and Schottky parts from the measured total C_p , and the results are shown in Fig. 4(c) for four different magnetic fields. C_M displays field-dependence at low temperatures (< 10 K), suggesting short-range magnetic interactions in the system. A broad

maximum is observed in the $C_M(T)$ data [Fig. 4(c)] at around 25 K which remains unchanged with the application of magnetic fields, supporting frustrated nature of magnetism in this compound as mentioned in the context of some $4d$ and $5d$ transition metal based spin liquids^{36,41,42}. Unlike in charge insulators, C_M reveals a finite T -linear component at very low temperatures for the higher applied magnetic fields, shown in the inset of Fig. 4(c). This points towards gapless nature of the spin density of states or metal-like spinon Fermi surface in this compound^{15,41,43,44}. It should be noted that with decreasing field, the temperature range of linear C_M versus T is reduced [inset to Fig. 4(c)], and therefore, any perceptible linear dependence of C_M is missing for both $H = 0$ and 10 kOe fields. The magnetic entropy change S_M has been obtained by integrating the zero field $\frac{C_M}{T}$ with T , as indicated in Fig. 4(d). The percentage of magnetic entropy released is $\approx 40\%$ out of a maximum of $R\ln(2J + 1)$ with $J = 1$ corresponding to the hypothetical triplet state. The magnetic entropy release by $\text{Ba}_3\text{CdIr}_2\text{O}_9$ is clearly more than the Zn and Mg compounds but lesser than the Ca, Sr systems^{24,26}, placing it in between the two ends of the $6H$ hexagonal perovskite family.

E. ^{113}Cd NMR

Nuclear magnetic resonance is a useful local probe of magnetism in materials. General experience in insulating oxide-type materials shows that, in the bulk magnetic susceptibility, even small extrinsic Curie-like contributions can overwhelm the intrinsic terms, especially at low-temperatures. In such a situation, the shift of the NMR resonance and its dependence on temperature (in favorable cases where the hyperfine coupling is significant) tracks the intrinsic spin susceptibility. With this motivation, we have measured ^{113}Cd NMR spectra from 4 K to 300 K. Some representative spectra are shown in Fig. 5(a). The lineshape is not a single symmetric line but rather has additional peaks on either side of the main line. Whereas susceptibility and/or hyperfine coupling anisotropy can give rise to asymmetric lineshapes, this does not appear to be the cause in the present case. Another possibility is the presence of different local environments which is ruled out by the unique crystallographic site for Cd. Some extent of Cd/Ir anti-site disorder could be present though this is less likely due to the ionic size difference between the two. Then one possibility of lineshape anisotropy is due to the distribution of magnetic environments for the ^{113}Cd nuclei, caused by rotational and tilting distortions of the IrO_6 octahedra^{45,46}. The shift of the central line [with respect

to ^{113}Cd reference line, as indicated in Fig. 5(a)] at high-temperatures is about 405 ppm. With decreasing temperature, we find that the main resonance line remains nearly unshifted with temperature. The additional resonance lines (at higher and lower frequencies) also do not shift with temperature. One can notice some broadening with decreasing temperature and one can see that below about 20 K the additional peaks merge with the main resonance line. Therefore, below $T = 20$ K, the gradual smearing out of the lineshape-anisotropy with lowering temperature might then imply that the local environments progressively become more homogeneous as a result of weakened local distortions with decreasing temperature^{45,46}, which is consistent with the findings of temperature dependent XRD experiments [Fig. 1(a)]. Now what is the implication of the temperature-independent shift that we observe? In case there is a (transferred) hyperfine coupling between the Cd nuclei and the Ir local moments, the ^{113}Cd NMR shift (^{113}K) should track the spin susceptibility. Note that the bulk susceptibility has a weak Curie-Weiss temperature dependence at low temperatures. This might imply that the observed NMR K -shift is just a chemical shift and that there are no local moments. Another possibility is that there are indeed Ir-local moments present (as suggested by the bulk susceptibility) but the hyperfine coupling is very weak as Cd nuclei senses the Ir-local moments through overlap with Ir $5d$ orbitals via oxygen. The broadening observed at low temperatures, then, definitely comes from a dipolar interaction with the Ir moments.

Next, we present the variation of the ^{113}Cd NMR spin-lattice relaxation rate $1/T_1$ with temperature. This was determined from a single exponential fit of the recovery of the ^{113}Cd longitudinal nuclear magnetisation following a saturating pulse sequence. Interestingly, the data [Fig. 5(b)] show a linear $1/T_1$ versus T dependence upto 150 K. In conventional metals/fermi liquids a Korringa behaviour is expected with $K^2 T_1 T = S = \frac{\hbar}{4\pi k_B} \left(\frac{\gamma_e}{\gamma_n}\right)^2$, where K is the NMR Knight shift; γ_e and γ_n are the electronic and nuclear gyromagnetic ratios. In case of a metallic T -independent susceptibility, a linear $1/T_1$ with T is expected whereas in semiconductors/non-magnetic insulators, a stronger decrease of $1/T_1$ with T is expected. For our data, we find that $K^2 T_1 T/S$ is close to 1, implying a possible fermi liquid state in our sample. But this is clearly refuted from our resistivity data. On the other hand, spin liquids have quasiparticles with spin degrees of freedom but no charge degrees of freedom. Hence, the linear $1/T_1$ versus T [in the temperature range $T = 4$ -150 K, shown in Fig. 5(b)] is suggestive of a spinon fermi surface. The absence of any significant T -dependence of

^{113}K in the present case (though the bulk susceptibility is Curie-Weiss-like) has therefore to be attributed to a weak hyperfine coupling together with weak intrinsic Ir-local moments. After all, the effective magnetic moment per iridium as inferred from the Curie constant (see magnetization discussion in Section-C) is only about 17% of that expected for spin-1/2 paramagnetic Ir^{4+} moments.

IV. SUMMARY AND CONCLUSION

In conclusion, unlike the iso-structural $6H$ analogue $\text{Ba}_3M\text{Ir}_2\text{O}_9$ ($M = \text{Ca}, \text{Sr}$) compounds, $\text{Ba}_3\text{CdIr}_2\text{O}_9$ reveals closer realization to the elusive $J = 0$ state. The small spin-orbital moments per Ir likely develop through real intersite hopping and noncubic crystal distortions. Despite moderate AFM interactions between these Ir^{5+} moments, our combined ^{113}Cd NMR, heat capacity, and dc susceptibility results discern the absence of magnetic ordering down to at least 2 K, invoking the possibility of QSL-like ground state for this compound. Both the XPS valence band spectra and electrical resistivity measurements suggest gapped electronic structure of this compound, which mimics the dominance of SOC, as in other $5d$ iridates. On the other hand, within the spin sector, the linear temperature dependence of ^{113}Cd NMR spin-lattice relaxation rate and also the linear magnetic heat capacity at low T are suggested to arise from the gapless nature of spin excitations within this material. Further measurements at even lower temperatures would be extremely useful to establish the absence of static magnetic moments in the ground state.

V. ACKNOWLEDGEMENT

MSK thanks UGC, India for fellowship. AB and VK thank CSIR, India for fellowship. SR thanks Department of Science and Technology (DST) [Project No. WTI/2K15/74] and TRC, IACS for support. Authors thank Indian Institute of Technology, Bombay and Indian Association for the Cultivation of Science, Kolkata for support in research. Authors also thank Prof. Subham Majumdar of IACS for useful discussions.

* Corresponding author:mssr@iacs.res.in

- ¹ W. Witczak-Krempa, G. Chen, Y. B. Kim, and L. Balents, *Annu. Rev. Condens. Matter Phys.* **5**, 57 (2014).
- ² M. J. Lawler, A. Paramakanti, Y. B. Kim, and L. Balents, *Phys. Rev. Lett.* **101**, 197202 (2008).
- ³ D. Pesin and L. Balents, *Nat. Phys.* **6**, 376 (2010).
- ⁴ K. Matsuhira, M. Wakeshima, R. Nakanishi, T. Yamada, A. Nakamura, W. Kawano, S. Takagi, and Y. Hinatsu, *J. Phys. Soc. Jpn.* **76**, 043706 (2007).
- ⁵ H. Fukazawa and Y. Maeno, *J. Phys. Soc. Jpn.* **71**, 2578 (2002).
- ⁶ S. Nakatsuji, Y. Machida, Y. Maeno, T. Tayama, T. Sakakibara, J. van Duijn, L. Balicas, J. N. Millican, R. T. Macaluso, and J. Y. Chan, *Phys. Rev. Lett.* **96**, 087204 (2006).
- ⁷ B. J. Kim, H. Jin, S. J. Moon, J.-Y. Kim, B. -G. Park, C.S. Leem, J. Yu, T. W. Noh, C. Kim, S.-J. Oh, J.-H. Park, V. Durairaj, G. Cao, and E. Rotenberg, *Phys. Rev. Lett.* **101**, 076402 (2008).
- ⁸ S.J. Moon, H. Jin, K.W. Kim, W.S. Choi, Y.S. Lee, J. Yu, G. Cao, A. Sumi, H. Funakubo, C. Bernhard, and T.W. Noh, *Phys. Rev. Lett.* **101**, 226402 (2008).
- ⁹ B. J. Kim, H. Ohsumi, T. Komesu, S. Sakai, T. Morita, H. Takagi, and T. Arima, *Science* **323**, 1329 (2009).
- ¹⁰ G. Khaliullin, *Phys. Rev. Lett.* **111**, 197201 (2013).
- ¹¹ G. Cao, T. F. Qi, L. Li, J. Terzic, S. J. Yuan, L. E. DeLong, G. Murthy, and R. K. Kaul, *Phys. Rev. Lett.* **112**, 056402 (2014).
- ¹² M. A. Laguna-Marco, P. Kayser, J. A. Alonso, M. J. Martínez- Lope, M. van Veenendaal, Y. Choi, and D. Haskel, *Phys. Rev. B* **91**, 214433 (2015).
- ¹³ T. Dey *et al.*, *Phys. Rev. B* **93**, 014434 (2016).
- ¹⁴ M. Bremholm, S. E. Dutton, P. W. Stephens, and R. J. Cava, *J. Solid State Chem.* **184**, 601 (2011).
- ¹⁵ A. Nag, S. Bhowal, A. Chakraborty, M. M. Sala, A. Efimenko, F. Bert, P. K. Biswas, A. D. Hillier, M. Itoh, S. D. Kaushik, V. Siruguri, C. Meneghini, I. Dasgupta, and Sugata Ray, *Phys. Rev. B.* **98**, 014431 (2018).
- ¹⁶ O. N. Meetei, W. S. Cole, M. Randeria, and N. Trivedi, *Phys. Rev. B* **91**, 054412 (2015).
- ¹⁷ G. Chen, L. Balents, and A. P. Schnyder, *Phys. Rev. Lett.* **102**, 96406 (2009).
- ¹⁸ X. Liu. *et al.*, *Phys. Rev. Lett.* **109**, 157401 (2012).
- ¹⁹ S. Bhattacharjee, S.-S. Lee, and Y. B. Kim, *New J. Phys.* **14**, 073015 (2012).
- ²⁰ C. H. Kim, H. S. Kim, H. Jeong, H. Jin, and J. Yu, *Phys. Rev. Lett.* **108**, 106401 (2012).

- ²¹ T. Dodds, T. P. Choy, and Y. B. Kim, Phys. Rev. B **84**, 104439 (2011).
- ²² G. Jackeli and G. Khaliullin, Phys. Rev. Lett. **103**, 067205 (2009).
- ²³ D. I. Khomskii, K. I. Kugel, A. O. Sboychakov, and S. V. Streltsov, J. Exp. Theor. Phys. **122**, 484 (2016).
- ²⁴ A. Nag, S. Middey, S. Bhowal, S. K. Panda, R. Mathieu, J. C. Orain, F. Bert, P. Mendels, P. G. Freeman, M. Mansson, H. M. Ronnow, M. Telling, P. K. Biswas, D. Sheptyakov, S. D. Kaushik, V. Siruguri, C. Meneghini, D. D. Sarma, I. Dasgupta, and S. Ray, Phys. Rev. Lett. **116**, 097205 (2016).
- ²⁵ T. Sakamoto, Y. Doi, and Y. Hinatsu, J. Solid State Chem. **179**, 2595–2601 (2006).
- ²⁶ A. Nag, S. Bhowal, F. Bert, A. D. Hillier, M. Itoh, Ilaria Carlomagno, C. Meneghini, T. Sarkar, R. Mathieu, I. Dasgupta, and S. Ray, Phys. Rev. B **97**, 064408 (2018).
- ²⁷ T. Dey, M. Majumder, J. C. Orain, A. Senyshyn, M. Prinz-Zwick, S. Bachus, Y. Tokiwa, F. Bert, P. Khuntia, N. Büttgen, A. A. Tsirlin, and P. Gegenwart, Phys. Rev. B **96**, 174411 (2017).
- ²⁸ T. Dey, A. V. Mahajan, R. Kumar, B. Koteswararao, F. C. Chou, A. A. Omrani, and H. M. Ronnow, Phys. Rev. B **88**, 134425 (2013).
- ²⁹ J. Rodriguez Carvajal, Physica B **192**, 55 (1993).
- ³⁰ G. Cao, V. Durairaj, S. Chikara, L. E. DeLong, S. Parkin, and P. Schlottmann, Phys. Rev. B **76**, 100402(R) (2007).
- ³¹ Paula Kayser, María Jesús Martínez-Lope, Jose Antonio Alonso, María Retuerto, Mark Croft, Alexander Ignatov, and Maria Teresa Fernández-Díaz, Eur. J. Inorg. Chem. **2014**, 178–185 (2013).
- ³² G. Cao, A. Subedi, S. Calder, J.-Q. Yan, J. Yi, Z. Gai, L. Poudel, D. J. Singh, M. D. Lumsden, A. D. Christianson, B. C. Sales, and D. Mandrus, Phys. Rev. B **87**, 155136 (2013).
- ³³ Brendan J. Kennedy *et al.*, J. Solid State Chem. **123**, 14–20 (1996).
- ³⁴ V. K. Dwivedi, A. Juyal, and S. Mukhopadhyay, Mater. Res. Express **3**, 115020 (2016).
- ³⁵ S. Yoshii, and M. Sato, J.Phys. Soc. Jpn. **68**, 3034 (1999).
- ³⁶ Y. Okamoto, M. Nohara, H. Aruga-Katori, and H. Takagi, Phys. Rev. Lett. **99**, 137207 (2007).
- ³⁷ T. Dey, A. V. Mahajan, P. Khuntia, M. Baenitz, B. Koteswararao, and F. C. Chou, Phys. Rev. B **86**, 140405(R)(2012)
- ³⁸ L. T. Corredor, G. Aslan-Cansever, M. Sturza, Kaustuv Manna, A. Maljuk, S. Gass, T. Dey, A. U. B. Wolter, Olga Kataeva, A. Zimmermann, M. Geyer, C. G. F. Blum, S. Wurmehl, and

- B. Büchner, *Phys. Rev. B* **95**, 064418 (2017).
- ³⁹ Abhishek Nag and Sugata Ray, *J. Magn. Magn. Mater.* **424**, 93–98 (2017)
- ⁴⁰ R. Kumar, D. Sheptyakov, P. Khuntia, K. Rolfs, P. G. Freeman, H. M. Rønnow, T. Dey, M. Baenitz, and A. V. Mahajan, *Phys. Rev. B* **94**, 174410 (2016).
- ⁴¹ L. Balents, *Nature* **464**, 199 (2010).
- ⁴² J. G. Cheng, G. Li, L. Balicas, J. S. Zhou, J. B. Goodenough, Cenke Xu, and H. D. Zhou, *Phys. Rev. Lett.* **107**, 197204 (2011).
- ⁴³ M. R. Norman, and T. Micklitz, *Phys. Rev. Lett.* **102**, 067204 (2009).
- ⁴⁴ Y. Shen, Y.-D. Li, H. Wo, Y. Li, S. Shen, B. Pan, Q. Wang, H. C. Walker, P. Steffens, M. Boehm, Y. Hao, D. L. Quintero-Castro, L. W. Harriger, M. D. Frontzek, L. Hao, S. Meng, Q. Zhang, G. Chen, and J. Zhao, *Nature (London)* **540**, 559 (2016).
- ⁴⁵ T. Dey, R. Kumar, A. V. Mahajan, S. D. Kaushik, and V. Siruguri, *Phys. Rev. B* **89**, 205101 (2014).
- ⁴⁶ T. Aharen, J. E. Greedan, C. A. Bridges, A. A. Aczel, J. Rodriguez, G. MacDougall, G. M. Luke, T. Imai, V. K. Michaelis, S. Kroeker, H. Zhou, C. R. Wiebe, and L. M. D. Cranswick, *Phys. Rev. B* **81**, 224409 (2010).

TABLE I. $\text{Ba}_3\text{CdIr}_2\text{O}_9$ refined structural parameters (space group: $C2/c$, $\alpha = \gamma = 90^\circ$, $\beta = 91.352^\circ$), $a = 5.8990\text{\AA}$, $b = 10.19745\text{\AA}$, $c = 14.74057\text{\AA}$, $R_p = 20.1$, $R_{wp} = 16.3$, $R_{exp} = 6.72$, and $\chi^2 = 5.88$

Atom	Site occupancy		x	y	z	$B(\text{\AA})^2$
Ba(1)	4e	0.5	0	-0.0042(6)	1/4	0.159(2)
Ba(2)	8f	1	0.0142(3)	0.3338(4)	0.0924(3)	0.396(2)
Cd	4a	1	0	0	0	0.181(4)
Ir	8f	1	-0.0167(2)	0.0043(3)	0.8439(5)	0.306(4)
O(1)	4e	0.5	0	0.5304(6)	1/4	1.1(3)
O(2)	8f	1	0.2834(6)	0.2542(8)	0.2411(6)	1.1(3)
O(3)	8f	1	0.0364(5)	0.8273(3)	0.1012(4)	1.1(3)
O(4)	8f	1	0.2985(3)	0.0843(2)	0.0752(8)	1.1(3)
O(5)	8f	1	0.7625(6)	0.0783(4)	0.0932(5)	1.1(3)

TABLE II. $\text{Ba}_3\text{CdIr}_2\text{O}_9$ refined structural parameters comparison between room temperature (300K) and at low temperature (4K)

Temperature(K)	Crystal structure	Bond-lengths	Intra-dimer Ir-Ir (\AA)	Inter-dimer Ir-Ir along c axis(\AA)	Inter-dimer Ir-Ir along $a-b$ plane (\AA)
300	S.G: $C2/c$ a = 5.8990 (\AA) b = 10.1974 (\AA) c = 14.7405 (\AA) $\beta = 91.352^\circ$	Ir-O1 (\AA) = 1.951 Ir-O2 (\AA) = 2.184, 1.998 Ir-O3 (\AA) = 1.840 Ir-O4 (\AA) = 1.915 Ir-O5 (\AA) = 1.984	2.75	5.73, 5.73, 5.76	5.890, 5.899
4	S.G: $C2/c$ a = 5.8752 (\AA) b = 10.1615 (\AA) c = 14.7145 (\AA) $\beta = 91.701^\circ$	Ir-O1 (\AA) = 1.946 Ir-O2 (\AA) = 1.987, 1.997 Ir-O3 (\AA) = 1.835 Ir-O4 (\AA) = 1.905 Ir-O5 (\AA) = 1.981	2.75	5.73, 5.73, 5.71	5.870, 5.875

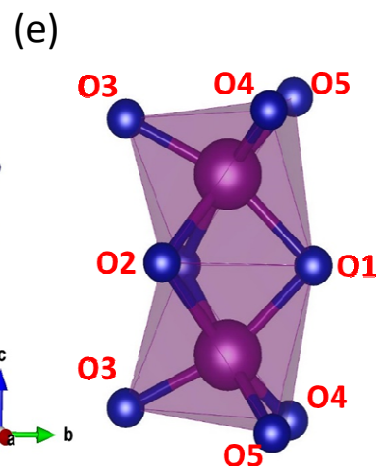
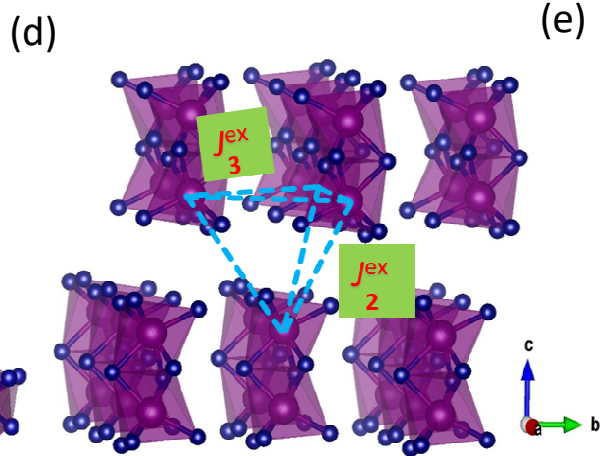
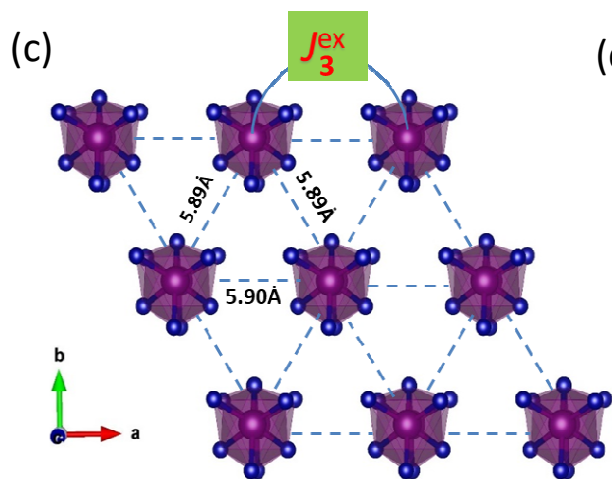
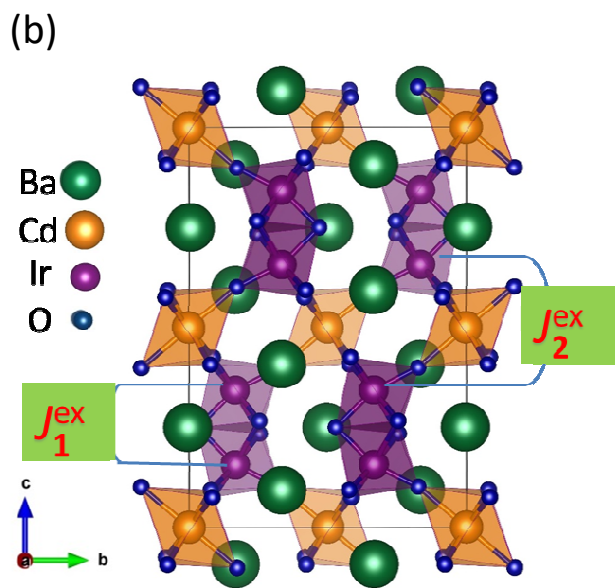
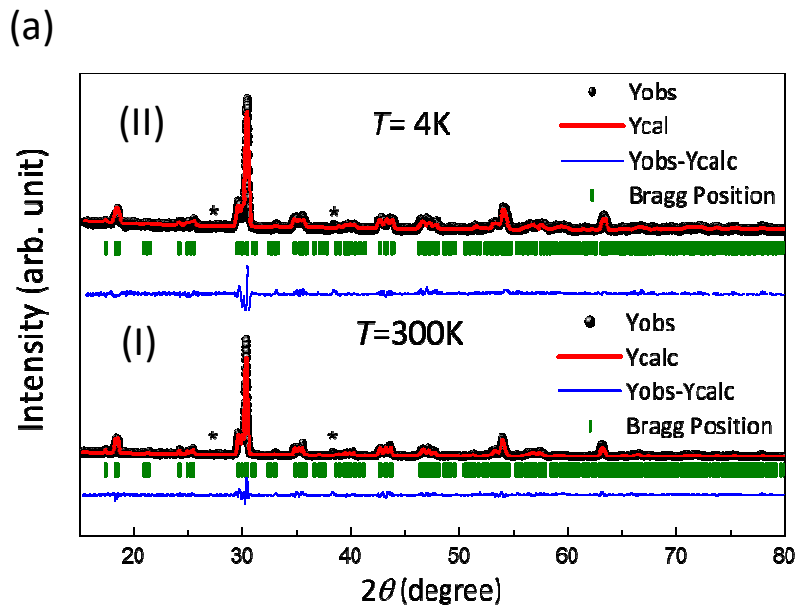
FIG. 1. (color online) Rietveld refined XRD pattern of $\text{Ba}_3\text{CdIr}_2\text{O}_9$ sample at 300K (a-I) and 4K (a-II); “*” denotes unidentified nonmagnetic impurity phase; (b) Refined crystal Structure, indicating exchange interaction paths; (c) Edge-shared frustrated Ir-triangular network in $a-b$ plane; (d) Frustrated Ir-triangular network along c axis; (e) Ir_2O_9 dimer unit consisting of two face-shared IrO_6 octahedra, and 5 different types of oxygen

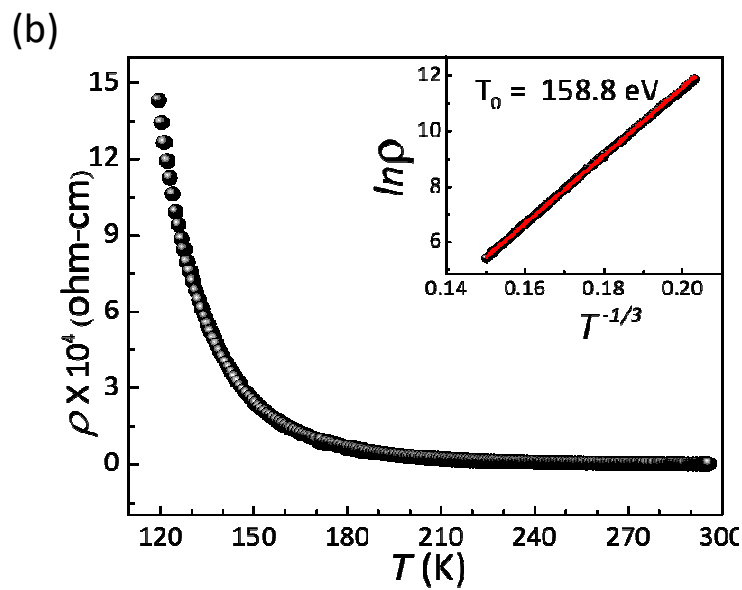
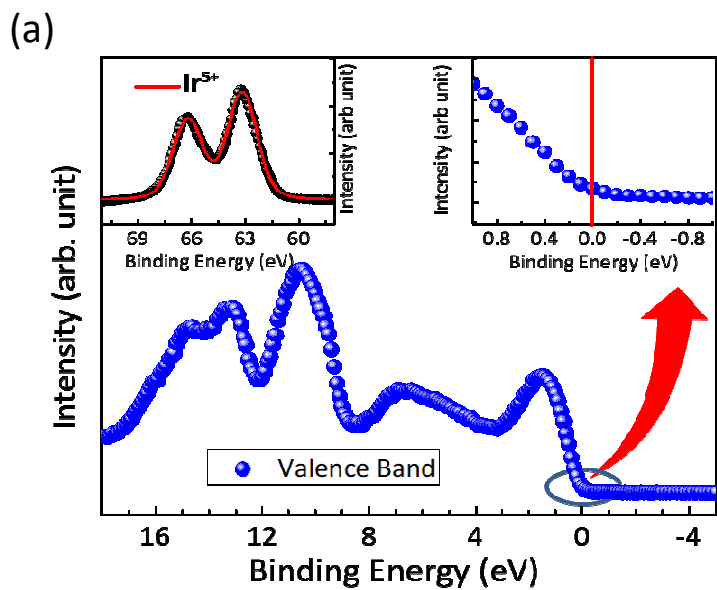
FIG. 2. (color online) (a) Valance band photoemission spectra for $\text{Ba}_3\text{CdIr}_2\text{O}_9$; Top right inset: expanded view of the valance band near the Fermi level; Top left inset: Ir $4f$ core level XPS spectrum (shaded black circles) along with the fitting (red solid line) (b) Temperature dependent zero field electrical resistivity variation, Inset: Respective Mott VRH fitting in 2- D

FIG. 3. (color online)(a)Temperature dependent dc susceptibility variations during zero-field-cooled (open blue circles) and field-cooled (shaded blue circles) protocols; Inset: Temperature dependence of $1/(\chi-\chi_0)$ is plotted,(b) Field dependence isothermal magnetization at 4 K and 300 K.

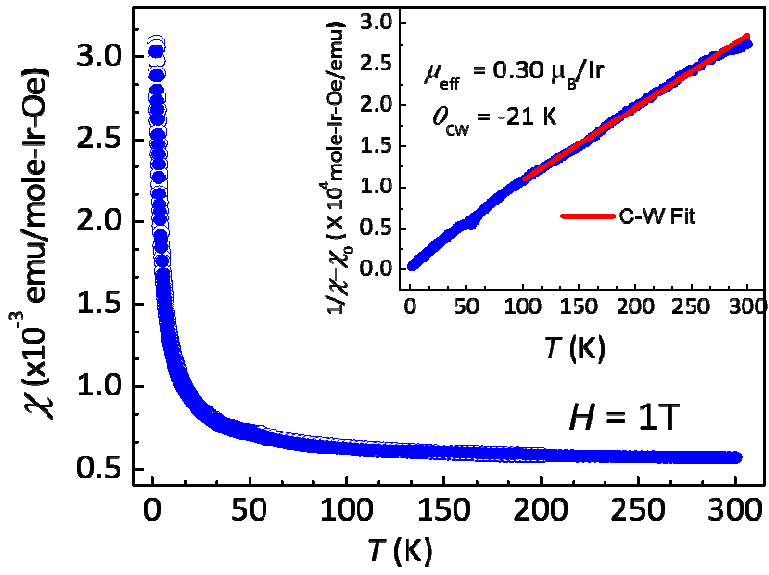
FIG. 4. (color online) (a)Temperature dependence of total specific heat C_p in low- T region for zero field and also several applied magnetic fields, Inset: Lattice contribution to the zero field C_p data; (b) Temperature variations of the T -divided $[C_p(H \neq 0) - C_p(H=0)]$ at several magnetic fields (shaded black circles) along with the two level Schottky anomaly fits(solid red lines), Top inset: Magnetic field dependence of the Schottky energy gap(Δ/K_B verses H , shaded black circles and the subsequent linear fitting(solid red line));(c) Temperature dependence of the magnetic specific heat C_M at zero field and the applied magnetic fields, inset: Zoomed-in views of the respective low- T linear $C_M - T$ variations; (d)Magnetic entropy loss as a function of temperature.

FIG. 5. (color online) (a) ^{113}Cd NMR line shapes at several temperatures (solid coloured lines) along with the ^{113}Cd reference (vertical dotted brown line), (b) Temperature dependence of the NMR spin-lattice relaxation rate (magenta half-filled circles) along with the linear fitting (solid orange line), error bars are also shown with the experimental data.





(a)



(b)

